AIP | Journal of Applied Physics

A comprehensive analysis of the contributions to the nonlinear optical properties of thin Ag films

Daniel T. Owens, Canek Fuentes-Hernandez, Joel M. Hales, Joseph W. Perry, and Bernard Kippelen

Citation: J. Appl. Phys. **107**, 123114 (2010); doi: 10.1063/1.3429118
View online: http://dx.doi.org/10.1063/1.3429118
View Table of Contents: http://jap.aip.org/resource/1/JAPIAU/v107/i12
Published by the American Institute of Physics.

A comprehensive analysis of the contributions to the nonlinear optical properties of thin Ag films

Daniel T. Owens,[1] Canek Fuentes-Hernandez,[1] Joel M. Hales,[2] Joseph W. Perry,[2] and Bernard Kippelen[1,a)]
[1]*Center for Organic Photonics and Electronics, School of Electrical and Computer Engineering, Georgia Institute of Technology, Atlanta, Georgia 30332, USA*
[2]*Center for Organic Photonics and Electronics, School of Chemistry and Biochemistry, Georgia Institute of Technology, Atlanta, Georgia 30332, USA*

(Received 16 December 2009; accepted 15 April 2010; published online 22 June 2010)

The nonlinear optical properties of 20 nm thick Ag films are investigated by time-resolved white-light continuum pump-probe experiments in both transmission and reflection mode. The dynamics of changes in permittivity $\Delta\varepsilon$ are measured at wavelengths between 500 to 700 nm. The data is fitted to a modified Drude model in the frequency domain and to a two-temperature model in the time domain. Changes in the individual Drude parameters are calculated as a function of time. A single, coherent model is proposed based on these fittings that describes the dynamics of the nonlinear optical properties of Ag, which could be used to model the nonlinear responses of multilayer structures containing thin films of Ag. The physical origins of the observed responses are discussed.
 [doi:10.1063/1.3429118]

I. INTRODUCTION

The nonlinear optical properties of noble metals have received great attention because the nonlinearity is orders of magnitude larger than in any other known material.[1–3] Silver in particular is interesting because the interband absorption peaks lie energetically above the visible spectrum, opening up the possibility of broadband applications in the visible portion of the spectrum.[4–8] The electronic and thermal properties that contribute to the nonlinearity, however, are not straightforward, and no fewer than five different processes contribute. These include both interband and intraband (free-electron) contributions, each of which include electron temperature and lattice temperature dependent components. All of these contributions are different from the relatively weak pure $\chi^{(3)}$ processes [on the order of 2×10^{-11} esu measured by third-harmonic generation at 1064 nm (Ref. 9)]. Understanding the source and nature of these contributions is essential to maximizing the effects of these nonlinear processes in more complex structures such as metal-dielectric photonic crystals[5,10,11] or induced transmission filters.[12,13]

A number of experimental investigations involving the steady state thermo-optic properties of Ag were carried-out in the 1970s that focused on both the temperature-independent[14–16] and temperature-dependent[17–21] optical properties. In these experiments the optical properties were probed by transmission or reflection spectroscopy, by ellipsometry, or by some combination thereof. These experiments combined with concurrent theoretical work provided good insight into how the inherent film structure affects the optical properties,[15,16,22,23] how the interband absorption spectrum is expected to change with temperature,[17–19] and what role electron-electron interactions might play.[14,20] However, these experiments were limited in that they were unable to distinguish effects that depend on the electron temperature from those that depend on the lattice temperature. Also, the dynamics of electron-electron and electron-phonon interactions could not be captured because these experiments were carried-out at steady state.

In more recent years, a number of femtosecond (fs) pump-probe experiments have been performed on thin silver films in order to measure the dynamics of the electrons.[24–29] Such experiments are difficult to perform because the thickness of the Ag film that can be measured for optical nonlinearity is limited by its reflectance and absorbance to less than 40 nm. However, the measurements that have been made give insight into the electron behavior, from the initially excited athermal electron distribution[25,26] to the rate of electron-phonon interaction[24] and the relative strengths of the interband and intraband contributions.[27] Investigations have also been made into the frequency dependent changes in the neighborhood of the interband transitions in the near UV (Ref. 28) and in the intraband contributions in the visible.[29] Still, it is difficult to attribute with certainty the physical origin of all of the observed nonlinear behaviors and precise quantitative measurements of the intraband contributions are lacking. With the present experiments we discuss current understanding of the origin of the nonlinear optical response of Ag while at the same time providing a simple model that can be used to predict this response when thin Ag layers, like the ones described in this paper, are incorporated into more complex multilayer structures.

The physical mechanisms that contribute to the nonlinear properties of Ag have, in general, different temporal and/or spectral contributions to either the real or imaginary part of the dielectric permittivity ε, so, in theory it should be possible to distinguish among these contributions from a single set of measurements provided they cover sufficiently large spectral and temporal ranges. To this end, we have

a)Author to whom correspondence should be addressed. Electronic mail: kippelen@ece.gatech.edu.

performed fs white-light continuum (WLC) pump-probe spectroscopy in both transmission and reflection modes on a thin (20 nm) film of Ag. From these measurements, with full knowledge of the structure, we determined ε across the spectral range of the white light continuum probe for times both during and after the interaction of the pump with the sample. Then we fit ε using a two temperature model in the time domain and a modified Drude model in the frequency domain. The Drude model was modified to take into account a limited amount of dispersion in the interband contribution. In so doing we were able to retain a simple model that can be numerically implemented and, at the same time, quantify the magnitudes and time scales of each contribution.

The rest of the paper is organized as follows: Sec. II describes the experimental methods used to fabricate and characterize the linear and nonlinear properties of Ag films; Sec. III gives the results of the measurements; and Sec. IV presents a discussion of the results, including the physical origin of each nonlinear contribution.

II. EXPERIMENTAL METHODS

A. Fabrication

All samples were fabricated on 0.16 mm thick glass cover slips that had been cleaned ultrasonically in soap, deionized water, acetone, and isopropanol for 15 min each. The films were deposited with a Kurt J. Lesker Axxis electron beam deposition system with a starting pressure of 1.3×10^{-6} Pa. The Ag and SiO_2 layers were deposited at a rate of 0.2 nm/s and the Ti layers at a rate less of than 0.02 nm/s, controlled manually in order to achieve subnanometer thickness. The samples were actively cooled and held at room temperature throughout the deposition. A "bulk" 160 nm thick Ag film was deposited as a reference sample. The samples to be measured for optical nonlinearity consisted of 20 nm thick layers of Ag covered by 50 nm thick layers of SiO_2, with a 0.25 nm thick Ti layer before and after the Ag to improve adhesion.[30]

B. Linear optical characterization

The linear optical properties of the samples were measured using a combination of spectroscopic ellipsometry, transmittance, and reflectance measurements. Ellipsometric measurements were made using a Woollam M2000 spectroscopic ellipsometer and transmission measurements were made using a Cary 5E UV/Vis/NIR spectrophotometer. Reflection measurements were made using a xenon light source and a monochromator; detection was accomplished by a pair of Si photodiodes for signal and reference that were connected to lock-in amplifiers. The standard sample used for reflection measurements was a 160 nm thick Ag film covered by 50 nm of SiO_2. The measurements were corrected to account for the fact that the reflectance of the standard is not exactly 100% but closer to 98%. The correction factor was calculated using the matrix transfer method applied to this structure, assuming a bulk refractive index for Ag. This resulted in the reflection data being adjusted upward by 1%–2% across the visible spectrum.

The permittivity of the thick Ag film was measured by spectroscopic ellipsometry. Typically, for a thin film of absorbing material, it is not possible to determine the complex permittivity and the thickness simultaneously using ellipsometry; however, since this film is thick enough to be fully opaque, the thickness is irrelevant and the complex permittivity can be fully determined.

The 20 nm thick Ag film is not fully opaque, so the permittivity cannot be uniquely determined using ellipsometry. For this reason, the permittivity was calculated from transmission and reflection data instead. The permittivity was fitted using an iterative numerical fitting routine based on the Newton–Raphson method in which the matrix transfer method was used to calculate the transmittance and reflectance of the structure. The starting point for the fitting routine was the measured bulk permittivity of Ag and, with each iteration, the permittivity was adjusted to minimize the discrepancy between the model and the measured data. In only a few iterations it was possible to match the model to within than the measurement error. This point by point fitting routine was repeated independently for each wavelength.

C. WLC pump-probe spectroscopy

The nonlinear optical properties were probed using a commercially available pump-probe spectroscopy system (Helios, Ultrafast Systems). A portion (~5%) of a laser beam from a Ti:sapphire regenerative amplifier (Spitfire, Spectra-Physics) operating at 800 nm and 1 kHz repetition rate provided the probe pulse to generate a WLC (WLC, 500–700 nm) while the remainder of the beam generated the pump pulse, tuned to either 550 or 650 nm by an optical parametric amplifier (TOPAS-White, Spectra-Physics). The pump beam was chopped at 500 Hz with a 50% duty cycle, with reference spectra being measured while the pump beam was blocked. The signal and reference data were averaged over a thousand measurements at each probe time delay, and a ΔOD spectrum was generated. The result was a wavelength versus time two-dimensional array of ΔOD values. The transmission mode measurements were converted to ΔT values based on the measured linear transmittance T_l according to

$$\Delta T = T_l(10^{-\Delta OD} - 1). \quad (1)$$

The process was repeated for reflection mode. The size of the pump beam at focus was measured using a knife-edge scan and yielded values of 260 μm (1/e radius) at 650 nm, 234 μm (1/e radius) at 550 nm, and the probe beam was 60 μm (1/e radius). Because the probe is significantly smaller than the pump, it is assumed that the probe overlaps with a region of constant (peak) fluence from the pump. A chirp correction factor was calculated by measuring the cross phase modulation response in the substrate, and the scattered pump light was subtracted based on measurements where the probe preceded the pump so that there was no observable nonlinear response of Ag. The pump pulse duration was 60 fs and the total instrument response time was 150 fs, precluding the possibility of investigating the initial athermal electronic behavior. For this reason, this work focused on time delays

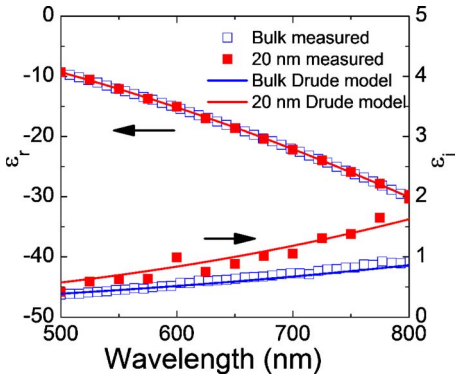

FIG. 1. (Color online) Measured complex permittivity of 160 and 20 nm Ag films with Drude model fits.

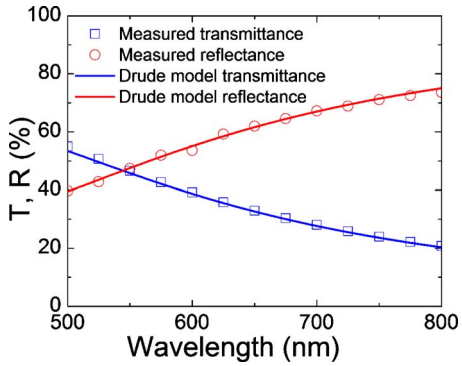

FIG. 2. (Color online) Measured transmittance and reflectance of 20 nm Ag film with Drude model fit.

larger than 1 ps, at which point the electrons are expected to have reached a thermal distribution.

III. EXPERIMENTAL RESULTS

A. Linear characterization

It is well known that the permittivity of Ag is dependent upon the deposition conditions;[16,31,32] thus, it is necessary to characterize each film individually. The frequency dependence of the permittivity in the visible region of the spectrum can generally be described by the Drude model

$$\varepsilon = \varepsilon_\infty - \frac{\omega_p^2}{\omega^2 + i\gamma\omega}, \tag{2}$$

where ε_∞ is the sum of the interband contributions, ω_p is the bulk plasma frequency, and γ is a damping constant. Equation (2) can be decomposed into its real and imaginary components, assuming $\gamma \ll \omega$

$$\varepsilon_r = \varepsilon_\infty - \frac{\omega_p^2}{\omega^2}, \quad \varepsilon_i = \frac{\gamma\omega_p^2}{\omega^3}, \tag{3}$$

where γ can be separated into a frequency independent term γ_l and a frequency dependent term β

$$\gamma = \gamma_l + \beta\omega^2. \tag{4}$$

Strictly speaking, ε_∞ is a function of frequency. Its dispersion could be calculated using the Kramers–Krönig relation from the interband absorption spectrum, though such calculations are beyond the scope of this paper and ε_∞ is approximated as a constant. This dispersion makes it difficult to fully separate the contributions of ε_∞ and ω_p to ε_r, as will be seen below.

The three temperature independent factors that most strongly affect the permittivity in the visible region of the spectrum are the density (void fraction) of the film,[15] the grain size,[15,16] and surface roughness.[14,16] The density governs the strength of the interband absorption and bulk plasma frequency ω_p, and the other two affect the free-electron damping parameter γ. Film thickness plays a significant role; the thinner the film, the more important surface roughness becomes.

The measured dispersion of the permittivity of the 160 nm thick Ag film is shown in Fig. 1. The permittivity was fitted to the Drude model with $\varepsilon_\infty = 4$, $\omega_p = 1.38 \times 10^{16}$ s^{-1}, $\gamma_l = 2.73 \times 10^{13}$ s^{-1}, and $\beta = 5.9 \times 10^{-18}$ s^{-1}. These numbers compare favorably with values from the literature $\omega_p = 1.36 \times 10^{16}$ s^{-1}, $\gamma_l = 2.73 \times 10^{13}$ s^{-1}, and $\beta = 5.8 \times 10^{-18}$ s^{-1};[20,33] ε_∞ differs significantly from the values of 2.7–3.4 reported in Refs. 14 and 20 though it agrees well with the value of 4 reported in Ref. 16. The variations in this value can be attributed in part to varying densities of the Ag films and to experimental errors either in the present measurements or the cited values; it should be noted that none of these measurements take into account dispersion in ε_∞.

It was shown in Ref. 16 that, in bulk Ag, if the grain size is smaller than the intrinsic mean free path (~52 nm), then γ will increase linearly with the inverse of the grain diameter. This arises from the fact that grain boundaries interrupt the free-flow of electrons, so the mean free path is limited by the diameter of the grains. The present value of γ is very close to the damping value of 2.6×10^{13} s^{-1} that would be expected from a large, perfect crystal of Ag, indicating that the grain size is on the order of 50 nm or more.

The bulk plasma frequency ω_p is defined as

$$\omega_p = \left(\frac{4\pi N e^2}{m^*}\right)^{1/2}, \tag{5}$$

where N is the density of free carriers, e is the electron charge, and m^* is the effective electron mass. Because ω_p is a function of carrier density, its value can be used to estimate the void fraction in the film. In view of Fig. 4 of Ref. 16, which plots the relationship between the void fraction and ω_p, it can be seen that the present film is essentially void free.

The permittivity and thickness values of the thin film that were to be used in the analysis of the optical nonlinearity measurements were calculated from transmittance and reflectance measurements shown in Fig. 2 by using the same fitting process as described above. The thickness was determined to be 19.7 nm and the permittivity was fitted to the Drude model with parameters identical to the bulk film except with $\gamma_l = 8 \times 10^{13}$ s^{-1}. This difference is due either to increased surface scattering in the thinner film or a smaller grain size. The complex permittivity is shown in Fig. 1. These values form the basis of the nonlinear characterization of these films by pump-probe spectroscopy.

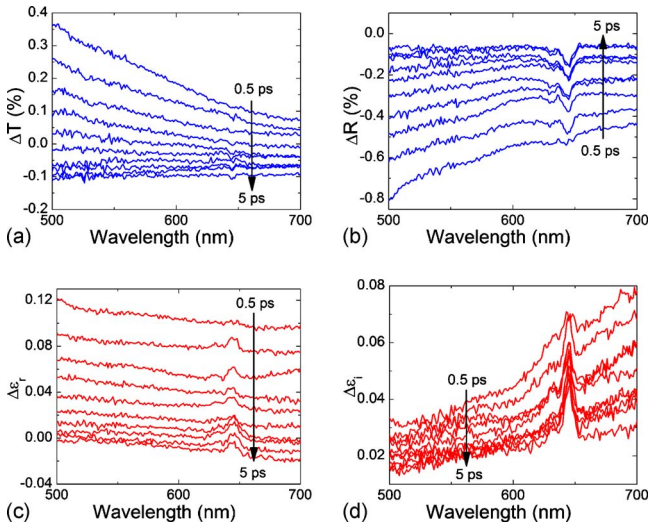

FIG. 3. (Color online) Evolution of (a) transmittance, (b) reflectance, (c) real part of permittivity, and (d) imaginary part of permittivity of 20 nm thick Ag film from 0.5 ps to 5 ps after 50 J/m^2 pulse.

B. WLC pump-probe spectroscopy

WLC pump-probe measurements were carried-out with incident fluences of 50, 37.5, 25, and 12.5 J/m^2 at a pump wavelength of 650 nm and 68 J/m^2 at 550 nm. Figure 3 shows the evolution of the nonlinear transmission and reflection of the 19.7 nm thick Ag film with a pump wavelength of 650 nm and a fluence of 50 J/m^2, starting at a delay of 0.5 ps and ending at a delay of 5 ps. The corresponding evolutions of ε_r and ε_i as shown in Fig. 3 were calculated using the same point by point fitting routine as for the linear data: at every wavelength and time delay the values of ε_r and ε_i were fitted to the modified transmittance and reflectance. This fitting is more robust than the commonly used method introduced by Rosei,[21,27] in which the change in permittivity is calculated directly from the gradients of the transmittance and reflectance because the present method takes the reflectances of the entire structure into account, not just that of the Ag film. Also, it is not limited to small perturbative changes. The features in the spectra at 650 nm in these measurements are caused by scattered light from the pump beam that could not be perfectly subtracted.

From this complex permittivity data the temporal and spectral behavior can be extracted. The temporal behavior can be described entirely in terms of the two-temperature model (TTM):[27]

$$C_e(T_e)\frac{dT_e}{dt} = -G_1(T_e - T_l) + P(t), \tag{6a}$$

$$C_l\frac{dT_l}{dt} = G_1(T_e - T_l) - G_2(T_l - T_a), \tag{6b}$$

where T_e, T_l, and T_a are the electron, lattice, and ambient temperatures, $C_e(T_e)=65\times T_e$ $[J/m^3\,K]$ is the temperature dependent electron specific heat, $C_l=2.4\times10^6$ $[J/(m^3\,K)]$ is the lattice specific heat, G_1 and G_2 $[W/(m^3\,K)]$ are the electron-phonon coupling and ambient coupling constants, and $P(t)$ $[W/m^3]$ is the absorbed power density. The equation for C_e holds for temperatures less than about 5000 K,[34] which is true for all measurements made here; the maximum electron temperature reached in the present experiments is on the order of 1400 K. Heat diffusion is neglected in the transverse dimension of the Ag film, which is assumed to have constant temperature. This is a good approximation because, with a Fermi velocity of 1.38 $\mu m/ps$,[16] there is sufficient time for the hot electrons to distribute through the thickness of the film at time scales shorter than can be resolved with the present setup. Lateral heat diffusion is included in the G_2 term of Eq. (6b). This term is included in the lattice temperature equation even though it is dominated by electron heat diffusion because electrons traveling near the Fermi velocity require on the order of 40 ps to traverse the probe region. Since it is assumed that the temperature seen by the probe is constant, thermal diffusion is only relevant at time scales longer than it takes for the electrons and phonons to reach thermal equilibrium. By including this term in the equation governing the lattice temperature instead of that for the electron temperature, spurious transient effects are avoided and the effective system behavior is captured. Figure 4 shows the TTM dynamics for each of the input fluences used, assuming initial temperatures $T_e=T_l=300$ K. These curves were calculated assuming that all the energy that is not transmitted or reflected is absorbed and converted directly into thermal energy in the electron motion.

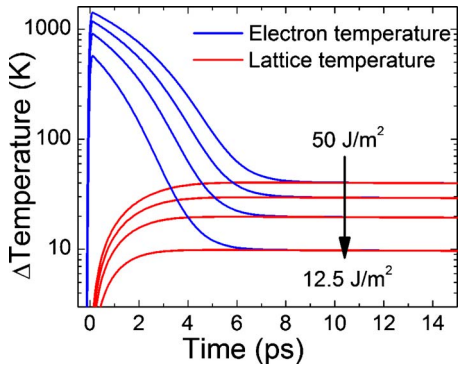

FIG. 4. (Color online) Evolution of electron and lattice temperatures of 20 nm thick Ag film calculated by the two temperature model for pump fluences 50, 37.5, 25, and 12.5 J/m^2 (semilog scale).

The coupling constants for the TTM were extracted from the decay rates of the complex permittivity shown in Fig. 3. These constants were extracted using a global fitting routine where the kinetics were assumed to be governed by similar decay processes across the different wavelengths and only the time constants were allowed to vary. Based on these measurements the electron-phonon coupling rate was found to be $G_1=3.0\times10^{16}$ $W/(m^3\,K)$, which is somewhat smaller than the value 3.5×10^{16} reported previously in the literature.[25,35] The rate of dissipation from Ag phonons to the surrounding environment is strongly dependent on the structure, film thickness, and dielectric material; in this particular film the rate is $G_2=5\times10^{14}$ $W/(m^3\,K)$.

In the frequency domain, the measured complex permittivity $\varepsilon_r+i\,\varepsilon_i$ was fitted at each time delay to the Drude model by allowing the parameters ε_∞, ω_p, and γ to vary with electron and lattice temperature. This was accomplished in

two stages. First, the response due to the electron temperature was extracted from the measurements in the neighborhood of 1 ps delay, at which time the change in electron temperature is near its maximum and the change in lattice temperature is still small. Second, the response due to the lattice temperature was extracted from the measurements after 6 ps, when the electrons have reached thermal equilibrium with the lattice, as shown in Fig. 4.

The response of ε_i is treated here first. At both time scales the response of ε_i was determined to be due primarily to the temperature dependence of γ, which can be described as

$$\gamma_1[T_l(t),T_e(t)] = 5.12 \times 10^{13} + (8.5 \pm 1.0) \times 10^{10} T_l(t) + (3.0 \pm 0.2) \times 10^{6} T_e^2(t). \quad (7)$$

The interband contribution to ε_i that has been investigated in depth in other studies[27–29] does not contribute to the present measurements because the interband contribution is highly localized around the interband transition frequencies, outside the range of the present measurements.

The response of ε_r is more complex because it involves contributions from both ε_∞ and ω_p. First, ω_p was assumed to be independent of electron temperature, so the response at 1 ps could be attributed solely to changes in ε_∞. This is physically reasonable because changes in ε_∞ should mainly arise from interband contributions while changes in ω_p could arise from effects such as band shifting that are more closely related to changes in the lattice temperature. Due to the Kramers–Krönig relation, changes in ε_i induce a spectral dispersion in ε_r that cannot be reproduced by assuming that ε_∞ is frequency independent. Including the exact contributions of the different interband transitions would add additional complexity to the model and is out of the scope of this paper. Instead a frequency dependent term is introduced

$$\varepsilon_\infty[\omega,T_e(t)] = 4 + [(3.0 \pm 0.2) \times 10^{-8} + (1.3 \pm 0.1) \times 10^{-39} \omega^2] \times T_e^2(t). \quad (8)$$

The frequency dependent term is in the form of a two-term Cauchy equation. This dispersion depends strongly on the fact that there is no electron temperature dependent component of ω_p; if such dependence exists, this dispersion will change significantly.

After 6 ps, changes in ε_∞ and ω_p, both contribute to the response of ε_r. Since both terms have a frequency dependence, it is difficult to distinguish between the two. However, there seem to be two different origins to changes in ε_r because the response changes from positive to negative at about 5 ps and because the response is stronger at lower frequencies after this point. Thus, it seems clear that changes in ε_∞ are not enough to explain the observed response of ε_r.

In order to place bounds on the relative magnitudes of the contributions of ε_∞ and ω_p, it was assumed that the slope of the dispersion of ε_∞ due to the change in lattice temperature would be greater than zero and within a factor of two of the dispersion due to electron temperature. The measured frequency dependence of ε_r was then fitted with ε_∞ and ω_p. If ε_∞ is assumed to be dispersionless, the resulting expressions are

$$\varepsilon_\infty[T_l(t)] = 3.94 + (1.7 \pm 1.2) \times 10^{-4} T_l(t), \quad (9a)$$

$$\omega_p[T_l(t)] = 1.374 \times 10^{16} + (1.8 \pm 0.5) \times 10^{11} T_l(t). \quad (9b)$$

If, on the other hand, the slope of the dispersion of ε_∞ is assumed to be double that of the electron temperature dependence, the resulting expressions are

$$\varepsilon_\infty[\omega,T_l(t)] = 3.94 + (0.4 + 6.0 \times 10^{-32} \omega^2) \times (1.5 \pm 1.0) \times 10^{-4} T_l(t), \quad (10a)$$

$$\omega_p[T_l(t)] = 1.374 \times 10^{16} + (1.6 \pm 0.4) \times 10^{11} T_l(t), \quad (10b)$$

where the dispersion term in ε_∞ was chosen so that its magnitude would be 1 in the center of the frequency range, so that the magnitudes of the dispersive and nondispersive temperature dependences can be directly compared. As expected, the uncertainty in these equations is quite large. However, it is apparent that uncertainty in the degree of dispersion in ε_∞ is less a contributing factor than the uncertainty in the measurements themselves. This is due to the fact that changes in ω_p appear to have a greater contribution to the nonlinear response than changes in ε_∞ after the electrons and lattice have reached thermal equilibrium. The dominance of ω_p also explains why there is a sign change in $\Delta\varepsilon_r$.

The constant terms in Eqs. (8), (9a), (9b), (10a), and (10b) were set so that at room temperature ($T_l = T_e = 300$ K) the Drude parameters would have the values $\varepsilon_\infty = 4$ and $\omega_p = 1.38 \times 10^{16}$ s^{-1} taken from the linear characterization measurements in the preceding section.

Equations (7), (8), (9a), (9b), (10a), and (10b) can be combined into a single set of equations to describe the full nonlinear response in terms of electron and lattice temperatures

$$\varepsilon_\infty[\omega,T_l(t),T_e(t)] = 3.94 + (0.7 + 3.0 \times 10^{-32} \omega^2) \times [(1.5 \pm 1.0) \times 10^{-4} T_l(t) + (4.3 \pm 0.5) \times 10^{-8} T_e^2(t)], \quad (11a)$$

$$\omega_p[T_l(t)] = 1.374 \times 10^{16} + (1.6 \pm 0.4) \times 10^{11} T_l(t), \quad (11b)$$

$$\gamma_1[T_l(t),T_e(t)] = 5.12 \times 10^{13} + (8.5 \pm 1.0) \times 10^{10} T_l(t) + (3.0 \pm 0.2) \times 10^{6} T_e^2(t), \quad (11c)$$

where, for ε_∞, the dispersion of the T_l term is assumed to be equal to the dispersion of the T_e term.

The temporal evolution of these parameters can be seen in Fig. 5 for a pump fluence of 50 J/m^2. As shown in Fig. 6, these equations describe the changes well in both the time and frequency domains for all pump fluences at both pump frequencies. This consistency confirms the fact that the observed effects are purely thermal in character. Hence, though there is some uncertainty in the exact magnitudes of the individual contributions, this set of equations can be used to describe the nonlinear optical response of a thin Ag film. As

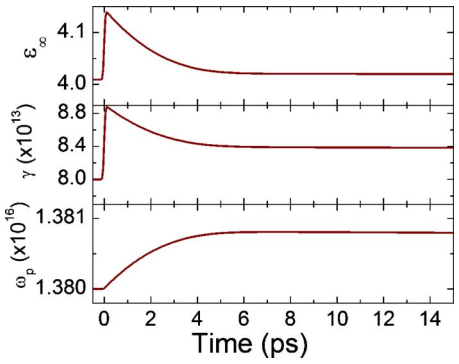

FIG. 5. (Color online) Evolution of Drude parameters ε_∞, (upper) γ, (middle) and ω_p (lower) in 20 nm thick Ag film for 50 J/m^2 pump fluence.

such, this model is useful for designing more complex multilayer structures incorporating this nonlinear optical response.

Further discussion of the nature and physical cause of each of these effects follows in Sec. III.

IV. DISCUSSION

There are at least five distinct contributions to the nonlinear response of a thin Ag film; these contributions correspond to the five temperature dependent terms found in Eq. (11). Figure 7 illustrates, using the model of a 50 J/m^2 pump pulse at 650 nm, how each of these terms contributes uniquely to the observed changes in the complex permittivity.

First, Figs. 7(a) and 7(b) show the distinction between the contributions to the permittivity that are dependent on the lattice temperature $T_l(t)$ and those dependent on the electron temperature $T_e(t)$. The change in permittivity was calculated as follows. First, $T_l(t)$ and $T_e(t)$ were calculated from the TTM (corresponding to the top curves of Fig. 4). From these, the Drude parameters were calculated using Eq. (11). For

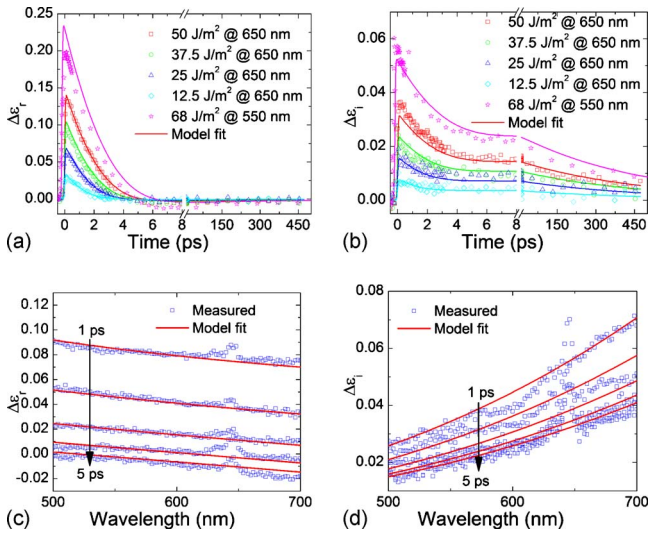

FIG. 6. (Color online) Evolution of (a) real and (b) imaginary parts of $\Delta\varepsilon$ of 20 nm thick Ag film with specified pump wavelength and fluence; probe wavelength is 500 nm. Solid lines represent Drude/TTM fits. (c) Real and (d) imaginary parts of $\Delta\varepsilon$ at various times after pump pulse for 50 J/m^2 pump at 650 nm.

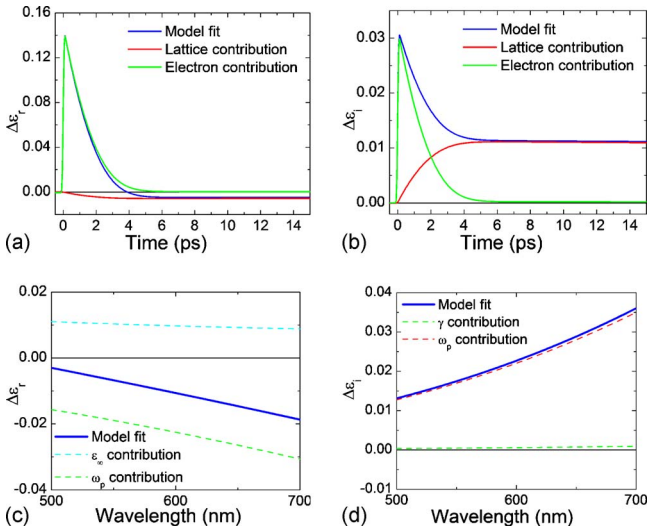

FIG. 7. (Color online) Evolution of (a) real and (b) imaginary parts of $\Delta\varepsilon$ of 20 nm thick Ag film over time for 50 J/m^2 pulse, and breakdown of electron and lattice contributions to nonlinearity. (c) Real and (d) imaginary parts of $\Delta\varepsilon$ 10 ps after pump pulse and breakdown of Drude parameter contributions to nonlinearity.

instance, $\varepsilon_\infty[\omega, T_l(t), T_e=300]$ was used to isolate the lattice temperature dependent contribution of ε_∞, and $\varepsilon_\infty[\omega, T_l=300, T_e(t)]$ was used to isolate the electron temperature dependence. The other two Drude parameters, ω_p and γ_1, were calculated similarly. The Drude parameters were then inserted into Eq. (3) to calculate the change in complex permittivity over time. It can be seen that before thermal equilibrium is reached the high temperature of the electron cloud produces a large effect but after equilibrium the lattice contribution is dominant.

Figures 7(c) and 7(d) show the contributions of each of the Drude parameters to ε_r and ε_i 10 ps, after thermal equilibrium between the lattice and electron cloud has been reached. Figure 7(c) shows that the contribution due to ω_p is dominant over that of ε_∞ in the response of ε_r, as was described earlier. Figure 7(d) shows that, while there is some slight contribution of ω_p to the response of ε_i, it is negligibly small. Thus, the assumption that the nonlinear response of ε_i can be calculated solely based on changes in γ is justified.

The physical cause of each contribution is now discussed in turn.

A. Interband effects

In the interband regime the behavior is typically attributed to three transitions. Two transitions, namely from the *d*-band to the *p*-band and from the *p*-band to the *s*-band, occur near the *L* point in the Brillouin zone;[17,18,27] the third transition is near the *X* point.[19,31] All of these transitions fall well inside the ultraviolet spectrum, so for applications in the visible spectrum the only observable effect is via the Kramers–Krönig relation. This is the ε_∞ term of ε_r.[14,26,31]

Several different temperature dependent interband effects contribute to the observed optical properties.[36] The first is Fermi smearing, in which the distribution of electron energies around the Fermi energy is spread out. This leads to a broadening of the absorption band with increasing

temperature[17,18,24,26,27] and an increase in the value of ε_∞. It has been shown[26] that the change in permittivity is proportional to the total energy contained in the electron cloud. An important distinction is that the energy is not directly proportional to the electron temperature because the electron specific heat is itself a function of temperature. Neglecting the electron-lattice coupling in Eq. (6a) and integrating gives

$$\frac{65\,T_e^2}{2} = E_e, \tag{12}$$

where E_e is the total thermal energy contained in the electron cloud. In terms of temperature, then, Fermi smearing follows T_e^2, as can be seen in Eq. (11a).

The second interband effect is band shifting, which is caused by thermal expansion in the silver crystals and follows the lattice temperature.[19] As the crystals heat up and expand, the energy levels of the valence and conduction bands, as well as the Fermi energy, shift. This leads to a corresponding shift in the absorption spectrum, which can again be observed in ε_∞ through the Kramers–Krönig relationship. The specific heat of the lattice is constant within this temperature range, so it is expected that this effect follows T_l; this again can be seen in Eq. (11a).

Other effects, such as those listed in Ref. 36 may contribute to the interband nonlinear response but in this wavelength range their effects cannot be separated from Fermi smearing and band shifting for the present set of measurements.

B. Intraband effects

The intraband regime is described by the Drude model, as shown above, with temperature dependent parameters γ and ω_p.

At least three mechanisms, electron-phonon scattering, electron-electron scattering, and electron-surface scattering contribute to γ. Electron-phonon scattering is the mechanism by which energy is transferred between electrons and the lattice and vice versa, and is the largest contribution to damping at room temperature. The scattering rate is proportional to the lattice temperature T_l due to an increase in the number of phonons.[14,24–27] Holstein's expression for the temperature dependence of electron-phonon interaction is[14]

$$\gamma_{e-ph} = \gamma_0\left[\frac{2}{5} + 4\left(\frac{T_l}{\Theta}\right)^5 \int_0^{\Theta/T_l} \frac{z^4 dz}{e^z - 1}\right], \tag{13}$$

where $\Theta = 220$ K is the Debye temperature. For $T_l > \Theta$, this equation can be approximated well by a linear function of T_l

$$\gamma_{e-ph} = \gamma_0(7.5 \times 10^{-2} + 4.43 \times 10^{-3} T_l). \tag{14}$$

The value for γ_0 can be extracted from the Drude parameters of bulk Ag, in the thermal range where the electron-electron contributions are negligible. As stated previously, $\gamma_1 = 2.73 \times 10^{13}$ s^{-1} for our bulk film, so $\gamma_0 = 1.94 \times 10^{13}$ s^{-1}. Assuming that this value holds for the 19.7 nm thick film as well, then $\Delta\gamma_1/\Delta T_l = 8.6 \times 10^{10}$ s^{-1} K^{-1}. This matches well with the calculated value of 8.7×10^{10} s^{-1} K^{-1} from Eq. (11c).

Electron-electron scattering is expected to have a thermal dependence based on T_e^2 (Ref. 14)

TABLE I. Summary of contributions to nonlinearity in Ag.

Source	Drude parameter	Interband/ intraband	Electron/ lattice	Effect observed in $\varepsilon_r/\varepsilon_i$
Fermi smearing	ε_∞	Interband	Electron	ε_r
Band shifting	ε_∞	Interband	Lattice	ε_r
Electron-phonon	γ_1	Intraband	Lattice	ε_i
Electron-electron	γ_1	Intraband	Electron	ε_i
Plasma frequency	ω_p	Intraband	Lattice	ε_r

$$\gamma_{ee} = \frac{1}{12}\pi^3 \Gamma \Delta (1/\hbar E_F)[(k_B T_e)^2 + (\hbar\omega/2\pi)^2], \tag{15}$$

where $\Gamma = 0.55$ is the average of the scattering probability over the Fermi surface, $\Delta = 0.75$ is the fractional Umklapp scattering, and $E_F = 5.5$ eV is the Fermi energy. Typically, the temperature dependent term is neglected because it does not become significant until $T_e > 1000$; since this threshold is exceeded in the present system, this temperature dependence must be considered. It follows from Eq. (15) that $\Delta\gamma/\Delta T_e^2 = 2.2 \times 10^6$ s^{-1} K^{-2}, compared to 2.9×10^6 s^{-1} K^{-2} from Eq. (11c). A surface scattering contribution may in part make up some of this discrepancy; it would require taking a series of measurements on samples with carefully controlled surface morphologies to verify this.

Surface scattering results from diffuse reflection of electrons off the surface of the film; the strength of this contribution is morphology and thickness dependent, affected particularly by the surface roughness.[15] This accounts for a large part of the difference in γ between the bulk Ag film and the thin Ag film; however, the nonlinear contribution is unclear.

The thermal dependence of ω_p is not a well documented phenomenon because it is difficult to distinguish from other thermal effects, as stated earlier. Different values have been reported at different temperatures, but the precision has been low.[20] Variations in ω_p have been attributed as the cause of certain "ringing" phenomena in nanoparticles, but it is difficult to quantify the effect from such experiments.[37] Considering Eq. (5), there are two possible explanations for the variation: a change in carrier concentration and a change in electron effective mass. Considering the thermal expansion of Ag, the carrier concentration might be expected to decrease with increasing lattice temperature. However, only an increase in ω_p is observed in the present experiments so this is not a sufficient explanation. It is possible that as the band structure changes the effective mass is also modified; the precise determination of the causes of this effect will require further experiments and is beyond the scope of this paper.

The contributions to the nonlinear response of Ag can be categorized in several different ways: (1) whether it arises from interband or intraband effects; (2) whether it is electron temperature or lattice temperature dependent; and (3) whether the observed change occurs predominantly in the real or imaginary permittivity. Table I gives a summary of the nature of each contribution.

V. CONCLUSION

The WLC pump-probe measurements presented in this paper were used to identify five different contributions to the nonlinear processes of Ag: Fermi smearing, band shifting, electron-phonon scattering, electron-electron scattering, and changes in bulk plasma frequency. Open questions remain about the contributions of electron-surface scattering and the cause of the shift in the bulk plasma frequency. The model developed based on these measurements describes well the behavior of a semitransparent 20 nm Ag sample under different pump fluences and excitation wavelengths. The results of this analysis will aid in the rigorous design of more complex structures that take advantage of the nonlinear optical properties of Ag, such as one dimensional metal-dielectric photonic crystals or induced transmission filters.

ACKNOWLEDGMENTS

We would like to thank Professor Seth Marder and his group for the use of their spectrophotometer. This work was partially funded by NSF through STC (Grant No. DMR-0120967), by ARO through Contract/Grant No. 50372-CH-MUR, by AFOSR (BIONIC Center Grant No. FA9550-09-1-0162), and AFOSR (Grant No. FA9550-09-1-0418).

[1]D. Ricard, P. Roussignol, and C. Flytzanis, Opt. Lett. **10**, 511 (1985).
[2]K. Uchida, S. Kaneko, S. Omi, C. Hata, H. Tanji, Y. Asahara, A. J. Ikushima, T. Tokizaki, and A. Nakamura, J. Opt. Soc. Am. B **11**, 1236 (1994).
[3]H. B. Liao, R. F. Xiao, J. S. Fu, and G. K. L. Wong, Appl. Phys. B: Lasers Opt. **65**, 673 (1997).
[4]M. J. Bloemer and M. Scalora, Appl. Phys. Lett. **72**, 1676 (1998).
[5]M. C. Larciprete, C. Sibilia, S. Paoloni, M. Bertolotti, F. Sarto, and M. Scalora, J. Appl. Phys. **93**, 5013 (2003).
[6]M. S. Sarto, F. Sarto, M. C. Larciprete, M. Scalora, M. D'Amore, C. Sibilia, and M. Bertolotti, IEEE Trans. Electromagn. Compat. **45**, 586 (2003).
[7]M. Scalora, M. J. Bloemer, A. S. Pethel, J. P. Dowling, C. M. Bowden, and A. S. Manka, J. Appl. Phys. **83**, 2377 (1998).
[8]M. Scalora,N. Mattiucci, G. D'Aguanno, M Larciprete, and M. J. Bloemer, Phys. Rev. E **73**, 016603 (2006).
[9]R. W. Boyd, *Nonlinear Optics*, 2nd ed. (Academic, New York, 2003).
[10]N. N. Lepeshkin, A. Schweinsberg, G. Piredda, R. S. Bennink, and R. W. Boyd, Phys. Rev. Lett. **93**, 123902 (2004).
[11]R. S. Bennink, Y.-K. Yoon, R. W. Boyd, and J. E. Sipe, Opt. Lett. **24**, 1416 (1999).
[12]G. Q. Du, H.-T. Jiang, Z.-S. Wang, and H. Chen Opt. Lett. **34**, 578 (2009).
[13]P. H. Berning and A. F. Turner, J. Opt. Soc. Am. **47**, 230 (1957).
[14]R. T. Beach and R. W. Christy, Phys. Rev. B **16**, 5277 (1977).
[15]D. E. Aspnes, E. Kinsbron, and D. D. Bacon, Phys. Rev. B **21**, 3290 (1980).
[16]F. Parmigiani, E. Kay, T. C. Huang, J. Perrin, M. Jurich, and J. D. Swalen Phys. Rev. B **33**, 879 (1986).
[17]R. Rosei, Phys. Rev. B **10**, 474 (1974).
[18]R. Rosei, C. H. Culp, and J. H. Weaver, Phys. Rev. B **10**, 484 (1974).
[19]P. Winsemius, F. F. van Kampen, H. P. Lengkeek, and C. G. van Went J. Phys. F: Met. Phys. **6**, 1583 (1976).
[20]G. R. Parkins, W. E. Lawrence, and R. W. Christy, Phys. Rev. B **23**, 6408 (1981).
[21]R. Rosei and D. W. Lynch, Phys. Rev. B **5**, 3883 (1972).
[22]D. E. Aspnes, Thin Solid Films **89**, 249 (1982).
[23]J. B. Smith and H. Ehrenreich, Phys. Rev. B **25**, 923 (1982).
[24]R. H. M. Groeneveld, R. Sprik, and A. Lagendijk, Phys. Rev. Lett. **64**, 784 (1990).
[25]R. H. M. Groeneveld, R. Sprik, and A. Lagendijk, Phys. Rev. B **51**, 11433 (1995).
[26]N. Del Fatti, R. Bouffanais, F. Vallée, and C. Flytzanis, Phys. Rev. Lett. **81**, 922 (1998).
[27]J. Y. Bigot, V. Halté, J.-C. Merle, and A. Daunois Chem. Phys. **251**, 181 (2000).
[28]N. Del Fatti, C. Voisin, M. Achermann, S. Tzortzakis, D. Christofilos, and F. Vallée, Phys. Rev. B **61**, 16956 (2000).
[29]A. Devižis and V. Gulbinas, Appl. Opt. **47**, 1632 (2008).
[30]A. Anders, E. Byon, D.-H. Kimb, K. Fukuda, and S. H. N. Lim, Solid State Commun. **140**, 225 (2006).
[31]H. Savaloni and A. R. Khakpour, Eur. Phys. J.: Appl. Phys. **31**, 101 (2005).
[32]H. Savaloni and M. Firouzi-Arani, Philos. Mag. **88**, 711 (2008).
[33]M. A. Ordal, L. L. Long, R. J. Bell, S. E. Bell, R. R. Bell, R. W. Alexander, Jr., and C. A. Ward, Appl. Opt. **22**, 1099 (1983).
[34]Z. Lin, L. V. Zhigilei, and V. Celli, Phys. Rev. B **77**, 075133 (2008).
[35]Y. Hamanaka, N. Hayashi, A. Nakamura, and S. Omi, J. Lumin. **76–77**, 221 (1998).
[36]R. Rosei, F. Antonang, and U. M. Grassano, Surf. Sci. **37**, 689 (1973).
[37]N. Del Fatti, C. Voisin, F. Chevy, F. Vallée, and C. Flytzanis, J. Chem. Phys. **110**, 11484 (1999).